Supplementary Materials

Probing Strain in Palladium Nanocrystals during Electrochemically-induced Phase Transitions

Clément Atlan[1,2,3*], Corentin Chatelier[1,2], Apinya Ngoipala[4], Kyle Olson[1,2,3], Arnaud Viola[3], Ewen Bellec[1,2], Michael Grimes[1,2], Bruno Gilles[5], Minaam Qamar[6], Matous Mrovec[6], Steven J. Leake[2], Joël Eymery[1], Tobias S. Schülli[2], Matthias Vandichel[4], Marie-Ingrid Richard[1,2*], and Frédéric Maillard[3*]

[1] *Université Grenoble Alpes, CEA Grenoble, IRIG, MEM, NRX, 17 rue des Martyrs, F-38000 Grenoble, France*

[2] *ESRF, The European Synchrotron, 71 Avenue des Martyrs, F-38000 Grenoble, France*

[3] *Univ. Grenoble Alpes, Univ. Savoie Mont Blanc, CNRS, Grenoble INP, LEPMI, 38000 Grenoble, France*

[4] *School of Chemical Sciences and Chemical Engineering, Bernal Institute, University of Limerick, Limerick, V94 T9PX, Ireland*

[5] *Univ. Grenoble Alpes, Univ. Savoie Mont Blanc, CNRS, Grenoble INP, SIMAP, 38000 Grenoble, France*

[6] *Interdisciplinary Centre for Advanced Materials Simulation (ICAMS), Ruhr-Universität Bochum, Bochum, 44780, Germany*

E-mail: clement.atlan@esrf.fr,mrichard@esrf.fr,frederic.maillard@grenoble-inp.fr

This Supplementary Information file includes Supplementary Section 1 to 13.

Contents

Supplementary Section 1: H_2 partial pressure equivalence in gas phase and electrochemical conditions

Electrode potential serves as means to control or measure H_2 fugacity, that will be approximated to the partial pressure in the considered pressure range.[1,2] Nernst equation provides a straightforward relation to connect the electrode potential to the partial pressure of H_2 at equilibrium. Considering the hydrogen evolution reaction in acidic electrolyte:

$$2H^+ + 2e^- \longleftrightarrow H_2\ (g) \tag{1}$$

the Nernst equation for the equilibrium potential of H^+/H_2 is expressed as:

$$E_{H^+/H_2} = E^0_{H^+/H_2} + \frac{RT}{2F} \ln\left(\frac{[H^+]^2}{p_{H_2}/p_0}\right) \tag{2}$$

where, $E^0_{H^+/H_2}$ is the standard electrode potential versus the Standard Hydrogen Electrode (SHE), $[H^+]$ ($\mathrm{mol\,L^{-1}}$) is the concentration of protons (H^+), p_{H_2} is the partial pressure of molecular hydrogen (H_2), p_0 is the atmospheric pressure, and R ($R = 8.315\ \mathrm{J\,mol^{-1}\,K^{-1}}$), T (K) and F ($F = 96486\ \mathrm{C\,mol^{-1}}$) are the gas constant, the temperature and the Faraday constant, respectively. Note that the equilibrium potential E_{H^+/H_2} in the Nernst equation is referenced to the SHE. To express it relative to the Reversible Hydrogen Electrode (RHE), we establish the relation that links the two electrodes:

$$E_{RHE} = E_{SHE} + \frac{RT}{F} \ln([H^+]) \tag{3}$$

Usually, the expression $\frac{RT}{F} \ln(\ )$ is expressed at room temperature ($T = 298$ K) using $\log$ instead of $\ln$ such as: $\frac{RT}{F} \ln(\ ) = 0.059 \log(\ )$. In addition, we recall that pH is defined as
$\mathrm{pH} = -\log([H^+]) = -\ln([H^+])/\ln(10)$. Accordingly, the relation between RHE and SHE is expressed as a function of the pH:

$$E_{RHE} = E_{SHE} - 0.059\mathrm{pH} \tag{4}$$

Finally, because $E^0_{H^+/H_2} = 0$, rearranging Eq. 2 allows expressing the partial pressure of H_2 as a function of the electrode potential:

$$p_{H_2} = p_0 10^{\frac{-E_{RHE}}{0.03}} \tag{5}$$

$$\text{or generally, } p_{H_2} = p_0 e^{-E_{RHE}\frac{2F}{RT}}$$

The curve $p_{H_2} - E_{RHE}$ is depicted in Supplementary Figure **1** for potentials varying between 0 and 0.1 V, using an electrolyte with pH $= 1$[1]. The inset emphasises the exponential relationship and indicates the significant p_{H_2} change as the potential varies around 0.05 V. In particular, it is well established that phase transition between α and β phases occurs at potentials in a range between 0.05 and 0.06 V versus RHE.[3–6]

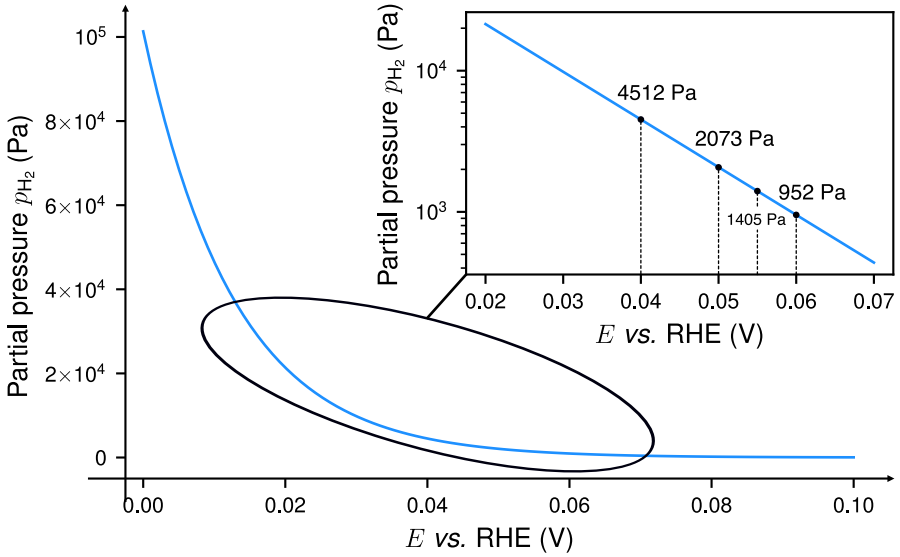

Supplementary Figure 1: **Equilibrium H_2 partial pressure as a function of the electrode potential.** The potential range is limited to $[0; 0.7]$ V, shown in a linear scale. The inset is a zoom of the potential range of interest $[0.02; 0.07]$ V and H_2 partial pressure is plotted in logarithmic scale. The pH of the considered electrolyte is 1.

[1] In this study, the pH is set at 0.96 as we used a 0.1 M H_2SO_4 electrolyte.

Supplementary Section 2: Radiolysis and beam-induced radical formation based upon Björling and co-workers's model

In this supplementary section, we introduce the model and equations developed by Björling et al.[7]

2.1 Model of the X-ray beam-induced radiolysis

Primary radiolysis is a phenomenon involving absorption of photons, leading to the ionisation of water molecules. This process generates several key species in acidic media, including $H^{\bullet}$, $OH^{\bullet}$, H_2O_2, and H_2 photoproducts. Primary radiolysis takes place within small regions known as spurs, situated around the location where X-ray absorption occurs. Typically, the rate of generation (measured in moles per litre per second, $\mathrm{M\,s^{-1}}$) is determined by empirical G-values, which represent the number of species formed per unit of energy absorbed ($\mu\mathrm{mol\,J^{-1}}$). Björling et al. developed a comprehensive model[7] that accounts for the generation and diffusion of these photoproducts, as well as their reactions with other chemical species.

In addition, the model is based upon cylindrical geometry problem. The X-ray beam is treated as cylindrical with an infinite focal depth. Consequently, species are assumed to diffuse solely perpendicular to the beam direction, and the distance from the beam centre, denoted as r, serves as the sole spatial dimension. The governing equation for the concentration C_i of species i, describing its diffusion in both space and time, is as follows:

$$\frac{\partial C_i(r,t)}{\partial t} = D_i \nabla^2 C_i(r,t) + v_{i,\text{ beam}} H(r_0 - r) + v_{i,\text{ reaction}} \quad \text{with} \quad i \in \{H^{\bullet}, OH^{\bullet}, H_2O_2, H_2\} \tag{6}$$

D_i represents the diffusion constant for the primary product of species i. $v_{i,\text{ beam}}$ stands for the generation rate of primary species i within the X-ray beam and ∇^2 is the Laplace operator. This generation rate is confined to the region within the beam radius (r_0), as governed by the Heaviside step function (H). There is no primary species generation beyond this boundary. $v_{i,\text{ reaction}}$ accounts for the rate of reactions occurring between species, leading to the formation of more stable species. These reactions mainly involve the primary photoproducts. Additionally, because our electrolyte is Ar-purged, we exclude reactions involving O_2. Here are the key reactions of interest, accompanied by their respective

rate constants:[8–11]

$$H_2 + OH^\bullet \rightarrow H^\bullet + H_2O \qquad 5 \times 10^7\ M^{-1}\,s^{-1} \tag{7}$$

$$H^\bullet + H_2O_2 \rightarrow H_2O + OH^\bullet \qquad 3.6 \times 10^7\ M^{-1}\,s^{-1} \tag{8}$$

$$OH^\bullet + H^\bullet \rightarrow H_2O \qquad 7 \times 10^9\ M^{-1}\,s^{-1} \tag{9}$$

$$2H^\bullet \rightarrow H_2 \qquad 5 \times 10^9\ M^{-1}\,s^{-1} \tag{10}$$

$$2OH^\bullet \rightarrow H_2O_2 \qquad 5 \times 10^9\ M^{-1}\,s^{-1} \tag{11}$$

Each reaction is characterised by its equilibrium coefficient, denoted as K_j, with j corresponding to a reaction listed above. These reactions are assumed to occur once the primary photoproducts have been generated. The law of mass action is applied to describe the production and consumption of a particular species:

$$v_{i,\text{ reaction}}(r,t) = \sum_j \nu_i K_j [A](r,t)[B](r,t) \tag{12}$$

Where ν_i represents the stoichiometric coefficient for species i in the specified reaction. It is positive if the species is a product and negative if it is a reactant.

To solve Equation 6 for each species i, we use the following boundary conditions:

$$\begin{cases} C_i(r,0) = 0 \\ \left[\frac{\partial C_i(r,t)}{\partial r}\right]_{r=0} = 0 \end{cases} \tag{13}$$

With these conditions in place, we can numerically solve the partial differential equation 6. The result is the spatially varying concentration of each species, $C_i(r,t)$, which allows us to compute the spatially averaged concentration, $\overline{C_i}(t)$. The concentration profiles are essential for assessing how each species evolves as a function of beam exposure time t. In the following section, we will discuss the curves of $\overline{C_i}(t)$, detailing the beam parameters used in our experiments.

While reaction rates and G-values are fixed, we have some flexibility in adjusting beam parameters to modify the photo-generation rate ($v_{i,\text{ beam}}$) of the photoproducts. The rate at which photoproducts are generated depends on (i) the energy provided by the photons (E_{photon}) and absorbed by the water (μ_{abs}), and (ii) the photon flux density (Φ, in number of photons per squared metre per second). Photon flux density is a function of both the photon flux (ϕ, in photons per second) and the beam section (S),

and is expressed as $\Phi = \frac{\phi}{S}$. For each species i with a G-value of G_i, the photo-generation rate is given by:

$$v_{i,\,\text{beam}} = G_i E_{\text{photon}} \mu_{\text{abs}} \Phi \tag{14}$$

$$v_{i,\,\text{beam}} \propto \Phi = \frac{\phi}{S} \tag{15}$$

2.2 Beam parameters

In practice, while photon energy E_{photon} is usually fixed at the beginning of a beamtime, optical slits can be employed to select smaller beam portions of various sizes. This approach not only improves the incident beam coherence but also reduces the photon flux ϕ as it selects the beam section before focalisation, while simultaneously increasing the size of the incident beam section S. Consequently, the photon flux density ($\Phi = \phi/S$) is effectively decreased by two factors: ϕ decreases and S increases, as the slit aperture decreases.

Supplementary Table **1** provides numerical examples that illustrate the relationship between slit aperture, photon flux, beam size, and photon flux density for a fixed photon flux in the direct beam (without any focusing optics), which is set at $3.152 \times 10^{11}\ \text{s}^{-1}$. One can notice that, at slit aperture of $90 \times 90\ \mu\text{m}^2$, photon flux density is almost ten times larger than that at slit aperture of $50 \times 50\ \mu\text{m}^2$.

Supplementary Table 1: **Beam parameters obtained at the ID01 beamline of ESRF, as a function of the slit aperture.**

Slit aperture	**Photon flux** (ϕ)	**Beam size** (S)	**Photon flux density** (Φ)
$50 \times 50\ \mu\text{m}^2$	4.955×10^9 photons s^{-1}	850 nm	$2.743 \times 10^{22}\ \text{s}^{-1}\,\text{m}^{-2}$
$60 \times 60\ \mu\text{m}^2$	7.136×10^9 photons s^{-1}	740 nm	$5.245 \times 10^{22}\ \text{s}^{-1}\,\text{m}^{-2}$
$70 \times 70\ \mu\text{m}^2$	9.712×10^9 photons s^{-1}	630 nm	$9.935 \times 10^{22}\ \text{s}^{-1}\,\text{m}^{-2}$
$80 \times 80\ \mu\text{m}^2$	1.269×10^{10} photons s^{-1}	510 nm	$1.928 \times 10^{23}\ \text{s}^{-1}\,\text{m}^{-2}$
$90 \times 90\ \mu\text{m}^2$	1.605×10^{10} photons s^{-1}	450 nm	$3.185 \times 10^{23}\ \text{s}^{-1}\,\text{m}^{-2}$

In this study, we set the photon energy at 19.9 keV, which is significantly higher than the 8.5 keV used by Björling et al.[7] This higher energy results in a 11-fold reduction in the water absorption coefficient,[12] and consequently, a roughly 4.7 times lower energy absorption rate ($E_{\text{photon}}\mu_{\text{abs}}$) due to

the increased energy per photon. Björling et al. employed a photon flux of $\sim 7 \times 10^{10}$ s^{-1} with a beam size of 113 nm, which led to a significantly higher photon flux density, exceeding all values provided in the table by at least two orders of magnitude: $\Phi_{\text{[Björling, 2023]}} = 2.2 \times 10^{25}$ $\mathrm{s}^{-1}\,\mathrm{m}^{-2}$.

2.3 Numerical analysis

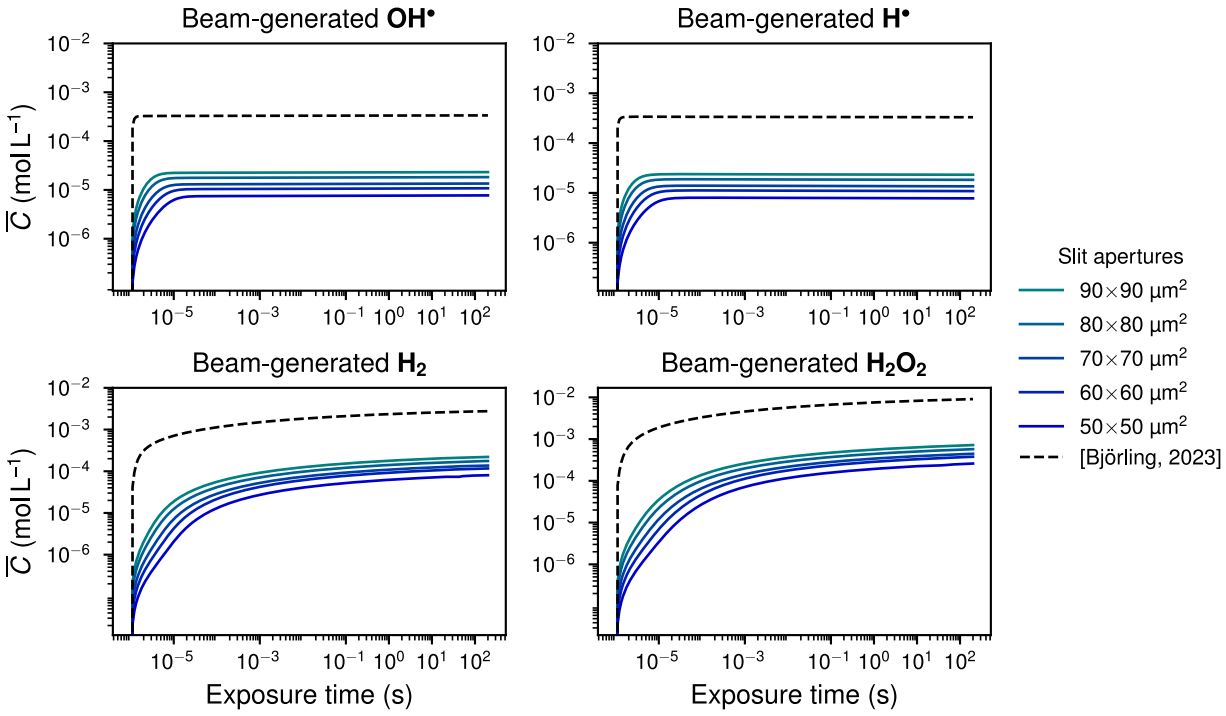

Supplementary Figure 2: **Radicals concentration due to beam-induced radiolysis of a** 0.1 **M H_2SO_4 electrolyte.** Species concentration as a function of the beam exposure time and for different beam parameters. The energy of the photons was 19.9 keV, only the slit aperture was the varying parameter. Dashed black lines correspond to the beam parameters provided by ref[7] : photon energy of 8.5 keV, photon flux of $\sim 7 \times 10^{10}$ s^{-1} and beam diameter of 113 nm.

Supplementary Figure **2** presents the concentration curves $\overline{C_i}(t)$ for each species ($i \in \mathrm{H}^\bullet, \mathrm{OH}^\bullet, \mathrm{H_2O_2}, \mathrm{H_2}$) as a function of beam exposure time, considering different slit apertures. The exposure time was set to 200 seconds, which is approximately the duration required for a BCDI scan acquisition during this experiment. For each generated species, there is an order of magnitude difference in concentration compared to the beam parameters used by Björling et al. This difference in concentration is crucial for our subsequent discussion regarding the influence of these species on a Pd NC. Interestingly, one could note that the entire process including primary radiolysis, diffusion and homogenous kinetics finally drives the evolution towards the two more stable species of $\mathrm{H_2O_2}$ and

H_2. As highlighted by Björling et al., $H^\bullet$ and $OH^\bullet$ are much more reactive radicals than H_2O_2 and H_2 species which do not settle in time but grow slower that $\log(t)$.

2.4 Towards an H_2 effective potential

In their study,[7] Björling et al. associated the α-to-β phase transition of Pd nanocrystals (NCs) with the presence of $H^\bullet$ radicals. More precisely, they proposed that this additional amount of H atoms can adsorb onto the surface of Pd NC, further leading to H absorption. By applying a significant overpotential, up to 0.5 V (depending on the photon flux), they could prevent the undesired α-to-β transition.

However, we note that the rate of reaction (9) (the transformation of $H^\bullet$ into H_2) is 100 times higher than its production in reaction (7) or its consumption in the production of H_2O and $OH^\bullet$ in reaction (8). Additionally, it is the partial pressure of H_2 that drives the α-to-β transition, and its concentration increases logarithmically with the beam exposure time, eventually reaching an order of magnitude higher than that of $H^\bullet$.

Considering H_2 as a direct contributing factor to the phase transition, we propose introducing the concept of effective potential of H_2, denoted as $E_{\mathrm{H_2,\,eff}}$. This effective potential refers to the local potential experienced by a Pd NC at its own scale. This potential accounts for both the additional H_2 species generated through radiolysis and the H_2 species in equilibrium with H^+ according to the Nernst equation. The partial pressure of the total amount of H_2 is defined such as: $p_{\mathrm{H_2,\,eff}} = p_{\mathrm{H_2}} + p_{\mathrm{H_2,\,beam}}$. The calculation of $E_{\mathrm{H_2,\,eff}}$ is determined by equation 16:

$$E_{\mathrm{H_2,\,eff}} = \frac{-RT}{2F} \times \ln\left(\frac{p_{\mathrm{H_2,\,eff}}}{p_0}\right) \tag{16}$$

Supplementary Figure **3a** presents the effective potential plotted against the applied potential for various slit apertures. This graph illustrates the potential shift caused by beam-induced radiolysis. As expected, the influence of the beam becomes less pronounced as the applied potential decreases. This is because the equilibrium partial pressure of H_2 (electrochemically-generated) increases exponentially as the potential decreases, as shown in Eq. 1. In panel **b**, we depict the evolution of the effective partial pressure of H_2 for different beam parameters. According to the model, the amount of H_2 generated by Björling et al.'s beam exceeds that generated by our beam by one order of magnitude. In addition, slit aperture of 90×90 μm^2 roughly doubles the partial pressure of H_2 compared to slit apertures of 50×50 μm^2.

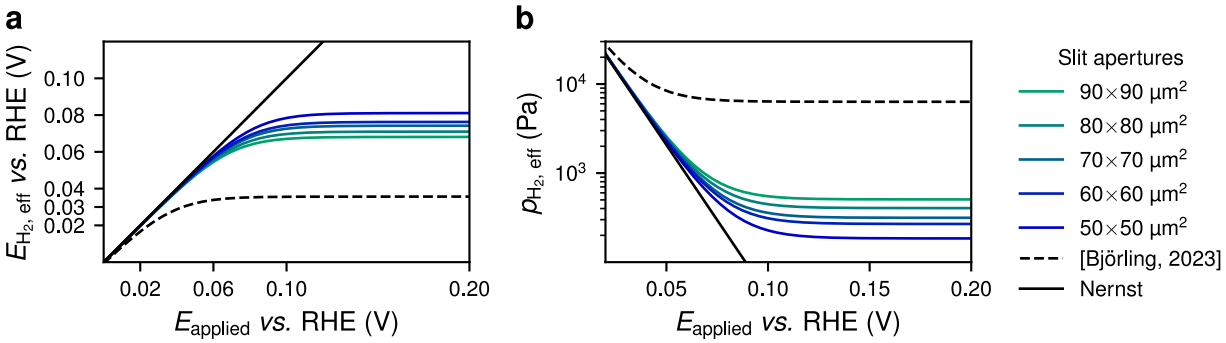

Supplementary Figure 3: **Variations of the effective potential and effective partial pressure in H_2 for varying slit aperture.** Panel **a**, the effective potential in H_2 as a function of the applied potential. The black line is the curve $y = x$ and serves as a visual guide to highlight the deviation from the applied potential. Panel **b**, plot of the partial pressure in H_2 defined as $p_{H_2,\,\mathrm{eff}} = p_{H_2} + p_{H_2\,\mathrm{beam}}$ to emphasise the deviation in H_2 partial pressure from the applied potential. The black line in panel **b** indicates the equilibrium partial pressure of H_2 derived from the Nernst equation, see 1. Legend on the right-hand side is valid for both panels. In our calculations, T was set to 298 K.

It should be noted that, according to this model, with a $50 \times 50\ \mu\mathrm{m}^2$ aperture, the effective potential stabilises around 0.08 V for applied electrode potentials $E > 0.08$ V. However, the current model has limitations, as it does not account for the renewal of the electrolyte at the NC surface driven by the peristaltic pump, nor the electrooxidation of H_2, the rate of which increases exponentially with the overpotential (see the Butler-Volmer equation and ref.[13]). Based on these considerations, we can state that:

- For $E < 0.08$ V, the electrochemical potential dominates, and the contribution of the beam to the total amount of H_2 is negligible.
- For $E > 0.08$ V, additional H_2 molecules are rapidly reoxidised[13] and/or flushed away by the electrolyte flow, which minimises any significant influence of the beam-generated H_2.

Thus, our experimental conditions ensure that in situ BCDI measurements can be conducted without significant interference from the X-ray beam.

Supplementary Section 3: Spatial resolution of the BCDI reconstruction

The resolution of the BCDI reconstructions was determined in all three main directions by analysing the line profile of the reconstructed amplitude. The derivative of the line profile was fitted by a Gaussian function and the associated full width at half maximum (FWHM) was calculated as FWHM $= 2.355\sigma$, σ being the standard deviation of the Gaussian function. Because the line profile includes two sharp changes –associated to the object opposed surfaces–, the resolution along one direction was calculated as the average of the two FWHMs provided by the Gaussian fits of the line profile derivative. The overall resolution was estimated at 31.5 nm.

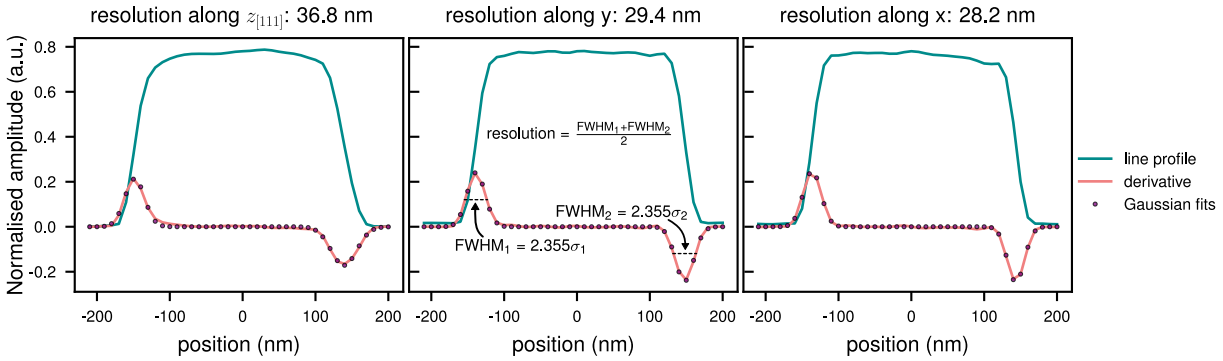

Supplementary Figure 4: Line profile of the reconstructed amplitude in z_{111}, y and x directions.

Supplementary Section 4: Determination of the H:Pd molar ratio

The amount of H that can be inserted into our Pd/GC sample was estimated using a coulometric method first introduced by Sherbo et al.,[14] later modified by Viola et al.[5] This methodology provides a means to quantify the average H content across various electrode potentials, although the H absorption behaviour at the individual NC level may exhibit slight deviations. The H loading, indicated by the H:Pd molar ratio, was assessed at various electrode potentials configuration by employing the following procedure:

1. **Electrochemical Impedance Spectroscopy (EIS):** EIS measurements were conducted at a fixed potential of $E = 0.4$ V, employing a potential step size of $\Delta E = 10$ mV, and sampling 20 frequencies spanning from 20 Hz to 100 kHz. The determination of the cell's Ohmic drop was essential, and typically this value was around $10\ \Omega$ in a 0.1 M H_2SO_4 solution. Compensation for the Ohmic drop, approximately 85% of the measured value, was dynamically adjusted using potentiostat.

2. **Conditioning:** This step ensures reproducible surface conditions for Pd/C nanoparticles before H insertion and de-insertion measurements. This protocol involved 400 CVs within the voltage range of 0.05 V to 0.50 V, all performed in an Ar-saturated electrolyte. Importantly, this procedure did not influence the Pd lattice due to the chosen values of the upper potential limit and the lower potential limit, which prevent anodic dissolution of Pd and the formation of the βphase, respectively.

3. **Electrochemical characterisation:** CVs were recorded within a voltage range spanning from 0.00 V to 0.60 V, utilising a potential sweep rate of $10\ \mathrm{mV\,s^{-1}}$.

4. **Coulometric quantification of H loading:** To quantify the H loading, chronoamperometric measurements were employed. Initially, H was inserted at various defined electrode potentials: $\{0.2; 0.1; 0.05; 0.04; 0.03; 0.02\}$ V. For each measurement, the potential was maintained for 10 minutes to ensure equilibrium was reached. Subsequently, H de-insertion was carried out using a CV from the insertion potential to 0.70 V at a scan rate of $10\ \mathrm{mV\,s^{-1}}$. The H desorption charge was estimated by integrating the area under the CV curve (*i.e.* the number of coulomb/electrical charge).

5. **Determination of the number of Pd moles:** The final step involved determining the number of moles of Pd on the examined sample. This was achieved by dissolving the Pd NPs in 'aqua regia', and then measuring the Pd concentration using an inductively-coupled plasma mass spectrometer (ICP-MS).

The molar ratios of hydrogen to palladium (H:Pd), plotted against the electrode potential, are shown in Supplementary Figure **5**. We observed that the transition from the α to β phase initiates below 0.05 V. At 0.04 V, the intermediate point evidences that the transition has started across the sample, with some NCs transitioning or fully transformed, while others are still in the α phase. At 0.03 V and lower, the NCs have all transformed. In ref.[15] , the authors reported H_2 partial pressures of transition from 3500 to 5000 Pa for NC sizes ranging from 180 to 330 nm, which corresponds to the potential range $[0.043; 0.039]$ V, according to Nernst equation, and therefore aligns with the present observations. Supplementary Fig. **5**b illustrates the same dataset in the form of an isotherm. Conversion from electrode potential to H_2 partial pressure was possible as the Pd NCs reached equilibrium at each measured point (see Methods). Accordingly, we observed a plateau indicative of the α-to-β phase transition around 0.04 V in Supplementary Fig. **5**b.

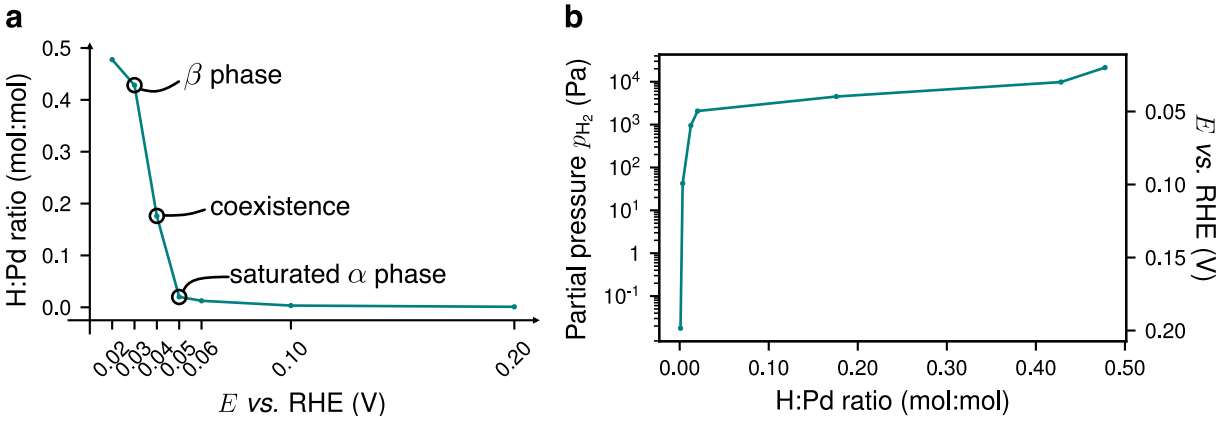

Supplementary Figure 5: **Evolution of the H:Pd molar ratio as determined by coulometry.** **a**, the H:Pd molar ratio as a function of the electrode potential. The potentials corresponding to the saturated α phase, the coexistence between α and β phases, and the pure β phase are indicated. **b**, the same data, but equilibrium H_2 partial pressure is plotted as a function of the H:Pd molar ratio. The corresponding equilibrium electrode potential is also given on the right-hand side y-axis. The relation between H_2 partial pressure and electrode potential is given by Eq. 1 at equilibrium. The coulometry was conducted at $T = 298$ K.

Supplementary Section 5: Reversibility of H insertion/de-insertion

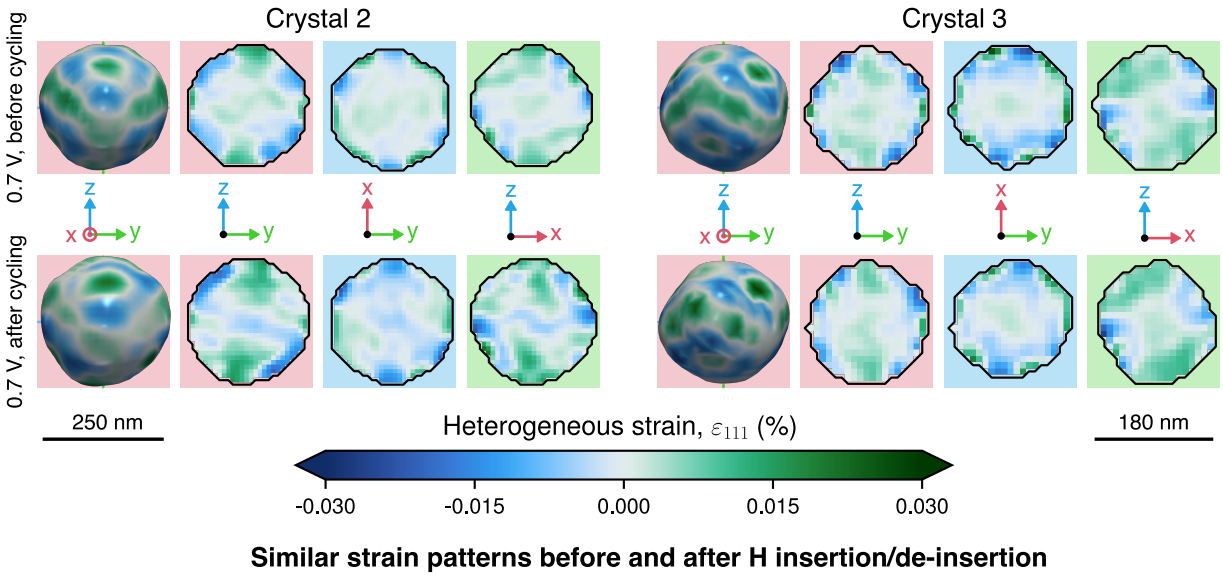

Supplementary Figure 6: **Similarity of strain patterns before and after H insertion and de-insertion.** The first four columns correspond to Crystal 2 and next four columns to Crystal 3. For each crystal, a 3D view and three slice views are plotted. The orientations are given by the tripod axis and the colour code. Red corresponds to X-axis and to the plane of normal X, blue to Z-axis and to the plane of normal Z and green to Y-axis and to the plane of normal Y. Colouring of the strain is identical for all views. Scales are different and indicated for each crystal.

Supplementary Section 6: Scanning electron micrograph

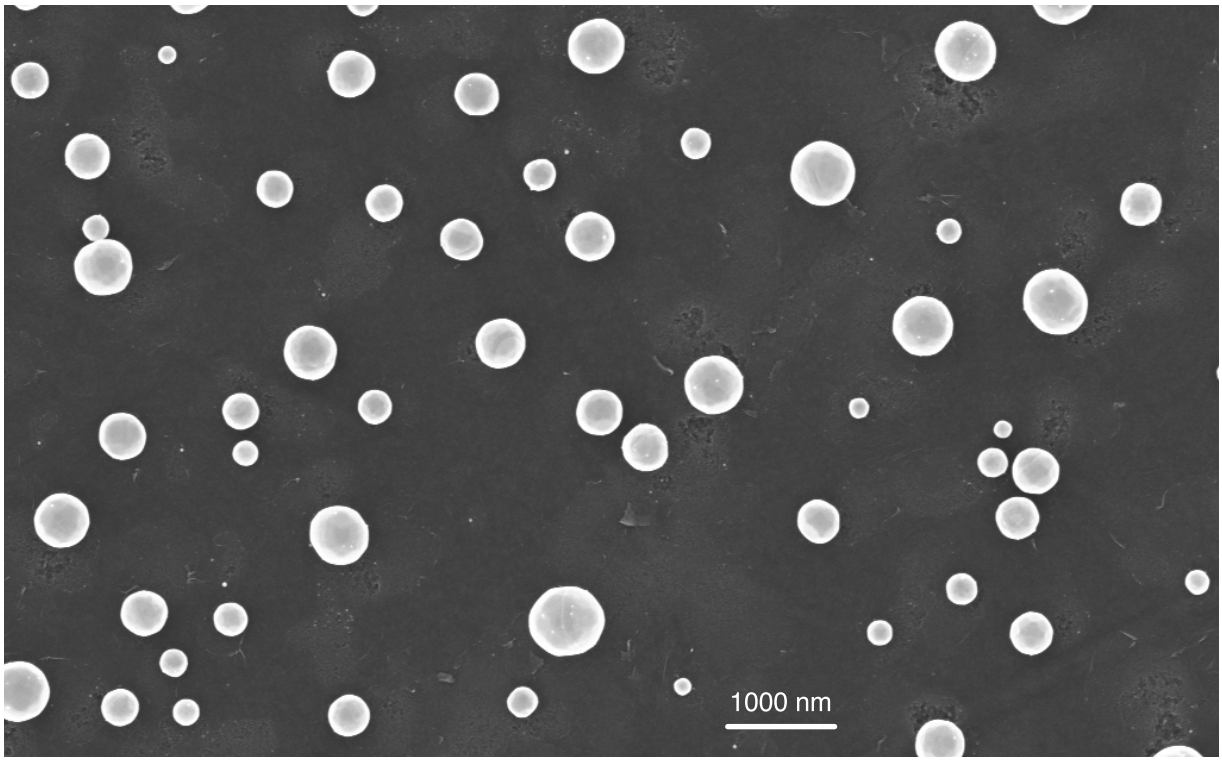

Supplementary Figure 7: Scanning electron micrograph of the Pd/GC sample used in this study. The sizes of the Pd nanoparticles range between 100 and 700 nm.

Supplementary Section 7: Summary table of the various NCs investigated

Since different Pd NCs were examined under different conditions, Table **2** summarises relevant information on the NCs investigated, their key characteristics, and the specific experimental conditions. Note that Crystal 4 was measured in a separate experiment using a different sample. Like Crystal 1, Crystal 4 did not fully recover its original morphology after H de-insertion, a phenomenon which we attribute to its size, as we will discuss later.

Supplementary Table 2: **Summary table of the various Pd NCs investigated in this study.** Crystal 1, 2, 3 and 4 were measured during the same beamtime. Photon energy was set to 19.9 keV for all measurement including Crystal 4.

Name	**Size** (nm^3)	**Shape**	**Description**
Crystal 1	$350 \times 350 \times 350$	spherical	This NC was used as a benchmark of the beam-generated H_2 species. The β phase nucleated at 0.2 V at a slit aperture of 90×90 $\mu\mathrm{m}^2$. The morphology of the NC could not be recovered after the H de-insertion.
Crystal 2	$250 \times 250 \times 250$	spherical, truncated cuboctahedron	BCDI tracking was performed on this NC using a slit aperture of 60×60 $\mu\mathrm{m}^2$. Major part of this study focuses on this NC.
Crystal 3	$180 \times 180 \times 180$	spherical, truncated cuboctahedron	The NC served as a control specimen and was measured only before and after the insertion/de-insertion cycle (Supplementary Figure **6**). We employed a slit aperture of 60×60 $\mu\mathrm{m}^2$ when measuring this NC.
Crystal 5	$360 \times 380 \times 380$	no particular shape, rather spherical	Investigated under 'fast' rocking curve, this NC was used to study the α-to-β and β-to-α phase transitions with low X-ray doses. A section is dedicated to Crystal 5 in Supplementary Section 13. We employed a slit aperture of 60×60 $\mu\mathrm{m}^2$ when measuring this NC.
Crystal 4	$350 \times 350 \times 225$	bean-like	This NC was measured during a different beamtime (same photon energy), and the slit aperture is unkown. BCDI tracking was also performed. The morphology of the NC could not be recovered after the cycling, but was still reconstructible (Supplementary Section 11).

Supplementary Section 8: Reciprocal space analysis upon α-to-β transition

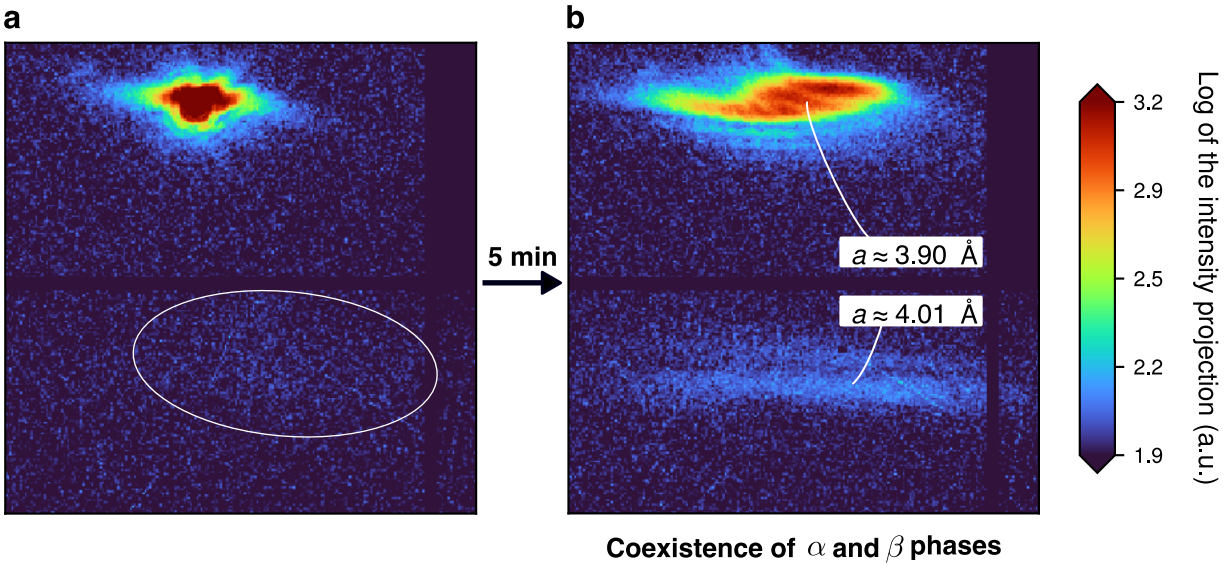

Supplementary Figure 8: **Projections of Crystal 2's diffraction patterns at** 0.06 **V.** For both panels, the projection corresponds to the summation of all rocking curves frames in order to enhance the signal features. Panel **a** corresponds to the first scan where large changes in the diffraction pattern occur, indicative of the onset of the α-to-β phase transition. The white ellipsoid indicates a region of highly diffuse scattered intensity. Panel **b** corresponds to another BCDI scan measured five minutes after the first, under the same experimental conditions. The diffraction pattern exhibits two distinct Bragg intensities, each associated with different lattice parameters, indicating the coexistence of α and β phases.

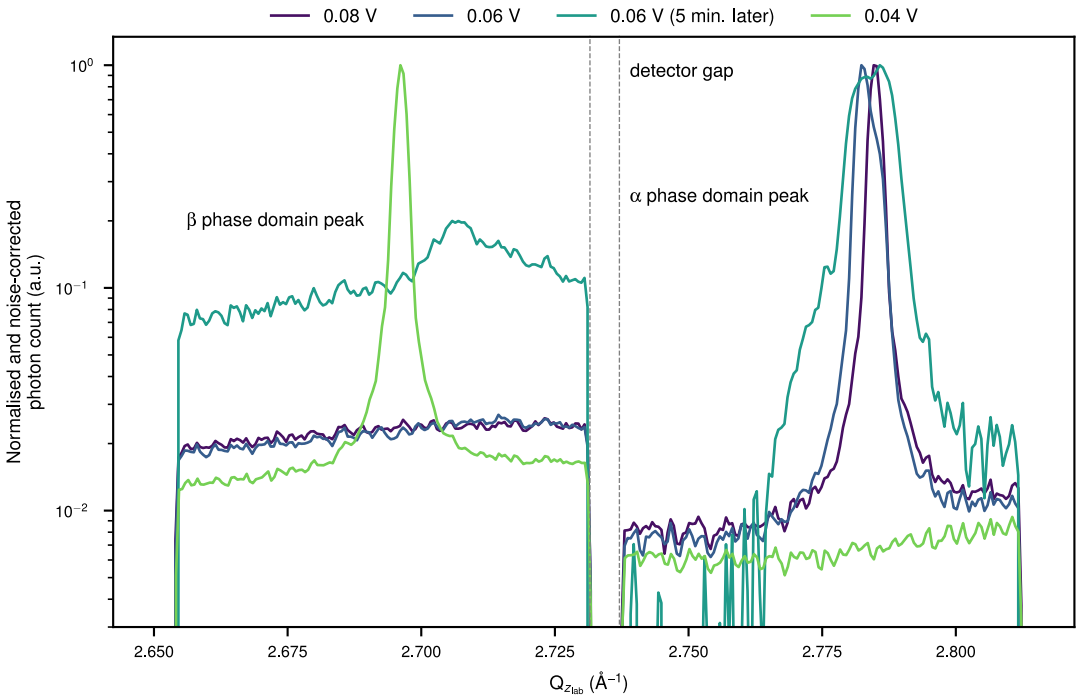

Supplementary Figure 9: **Diffracted intensity analysis at varying electrode potentials.** The detector intensity has been summed in the rocking curve and detector horizontal directions and are plotted against the vertical direction in the reciprocal space. For each scan, the integrated intensity was normalised to its maximum value. To emphasise fluctuations at low intensity levels, values corresponding to noise level were removed. The noise level is determined as the value with the highest number of occurrences in the intensity histogram.

Supplementary Section 9: Simulation pipeline

The first step of the pipeline consists in retrieving the surface data of the BCDI reconstruction and parsing it to the nanoSCULPT[16] software. To accurately populate the surface with the required atoms, the orientation matrix of the NC is required. The simulated system is then relaxed using LAMMPS[17] with the developed atomic cluster expansion (ACE) potential based on a PBE-D3 dataset. The structural relaxation employs the conjugate gradient method, with a stopping tolerance set to 10^{-10} eV normalised on the systems' total energy, and 10^{-10} eVÅ^{-1} for the atomic forces. PyNX[18] is subsequently employed to calculate the kinetic sum of the relaxed system at a given position in reciprocal space and generate the reciprocal space complex object (amplitude and phase), which can then be brought back to the direct space by performing an inverse Fourier transform. Following this, the *cdiutils*[19] routine is utilised to handle phase manipulation (phase ramp and offset), as well as calculate heterogeneous strain, *d*-spacing, and other relevant quantities.

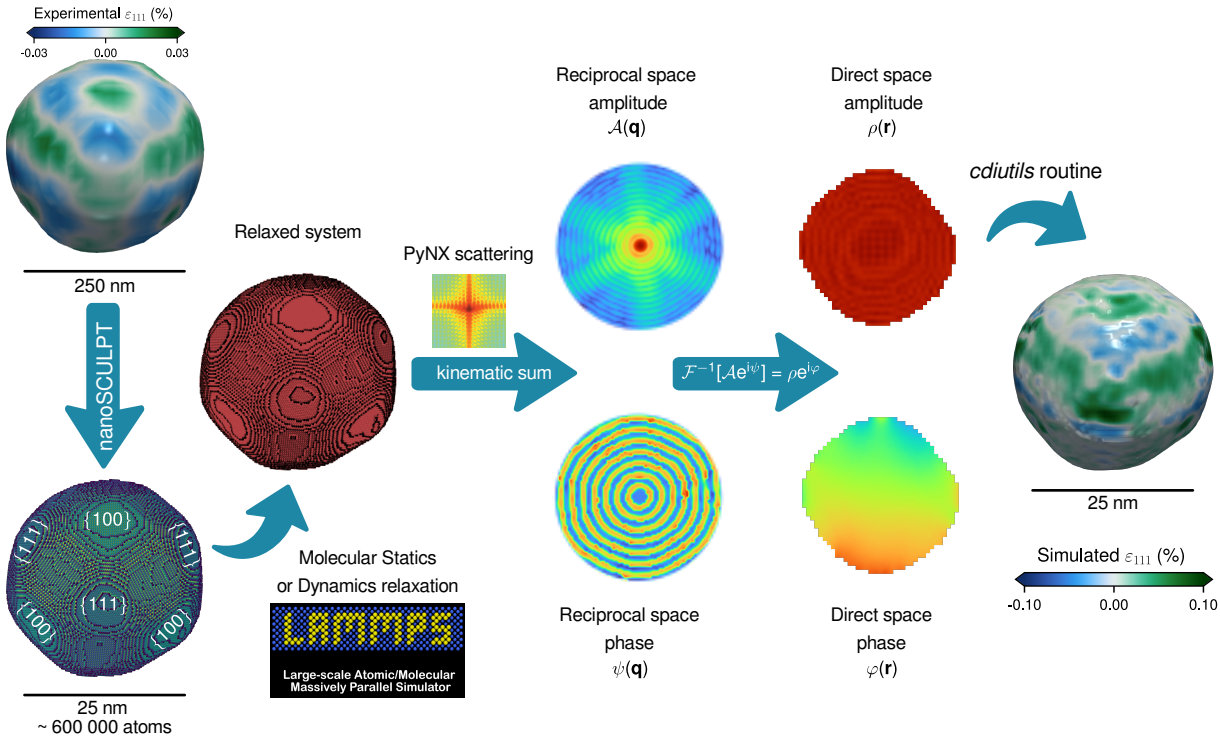

Supplementary Figure 10: Simulation pipeline, from the experimental shape to the simulated BCDI-like image.

Supplementary Section 10: Molecular Statics potential development

In this study, energy minimisation was performed using LAMMPS [17] with the ML_PACE package. [20] The interatomic interactions were described using the ACE [21] potential, parametrised and iteratively trained for the Pd–H system based on an extensive, representative set of PBE-D3 calculations containing both elemental phases of Pd and H, as well as binary structures of various compositions using the Pacemaker package. [22,23] Comprehensive details of the ACE model, its parametrisation and computational benchmarks will be presented in a follow-up study. The ACE potential employed in this study was initially validated to ensure its ability to properly describe the hydrogen diffusion, ad– and absorption processes in Pd systems, whose lattice parameter increases with increasing H:Pd ratio.

The formation of a bulk Pd hydride (PdH_x) was examined by initially populating H in the octahedral sites (for $x \leq 1$) of an fcc bulk Pd crystal, followed by filling the tetrahedral sites. The formation energies (E_{form}) for different Pd:H ratios were calculated as:

$$E_{\text{form}} = E_{\text{PdH}_x} - \left(N_{\text{Pd}} E_{\text{Pd}_{1,\text{bulk}}} + \frac{N_{\text{H}}}{2} E_{\text{H}_2} \right), \tag{17}$$

where E_{PdH_x}, $E_{\text{Pd}_{1,\text{bulk}}}$, and E_{H_2} are the total energies of the PdH_x system, the bulk Pd atom, and the H_2 molecule, respectively. Here, $x = \frac{N_{\text{H}}}{N_{\text{Pd}}}$, where N_{Pd} and N_{H} are the numbers of Pd and H atoms in the considered system, respectively. The formation energy and change in volume calculated by ACE are compared with reference Density Functional Theory (DFT) [24] for bulk PdH_x at varying hydrogen concentrations (x) in Supplementary Figure **11**. The most stable H:Pd ratio is $1:1$, with the lattice constant (a) calculated as 3.886 Å for Pd and 4.082 Å for PdH_1 using the ACE potential, in good agreement with DFT results ($a = 3.891$ Å for Pd and 4.079 Å for PdH_1). [24]

Furthermore, the ACE potential was validated for H adsorption on Pd(111), Pd(100), and Pd(110) surfaces. The adsorption energies of hydrogen atom (H^*; where '*' denotes a surface-bound species), E_{ads}, were calculated for all three surfaces as:

$$E_{\text{ads}} = E_{\text{H}^*/\text{Pd}} - E_{\text{Pd, slab}} - \frac{1}{2} E_{\text{H}_2}, \tag{18}$$

where $E_{\text{H}^*/\text{Pd}}$, $E_{\text{Pd, slab}}$, and E_{H_2} are the total energies of the Pd slab with adsorbed H, the clean Pd slab, and the H_2 molecule, respectively. Supplementary Figure **12** depicts the adsorption energies of H atom

on the Pd(111), Pd(100), and Pd(110) surfaces at different adsorption sites, calculated using ACE and DFT.[25] The ACE-potential seems to slightly overestimate the PBE-D3 adsorption energies for Pd(110) and Pd(100).

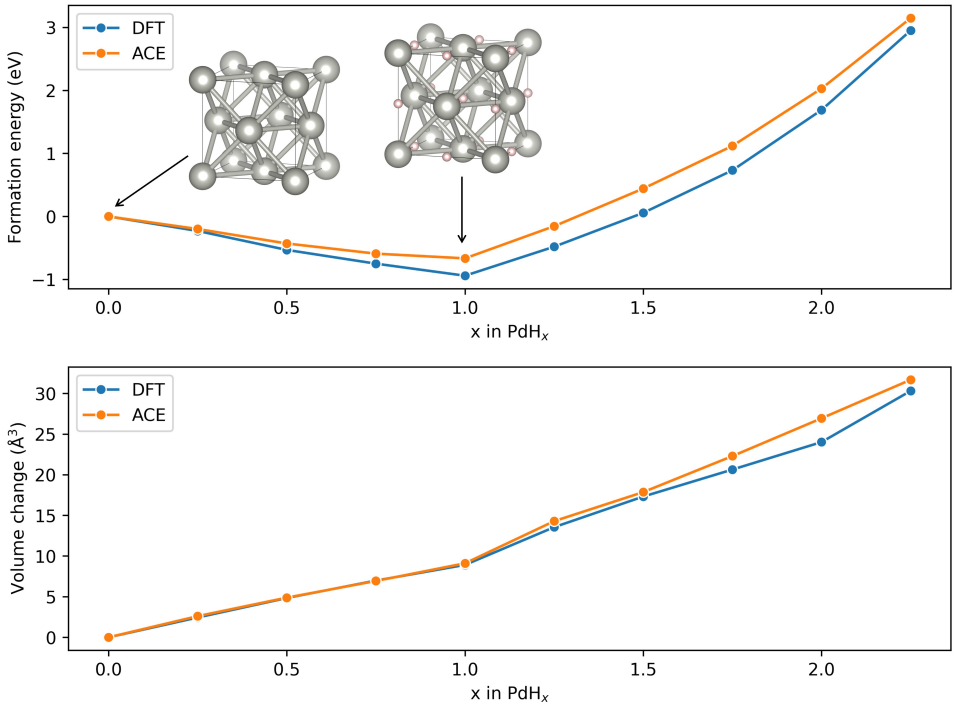

Supplementary Figure 11: Calculated formation energy and change in volume of a bulk PdH$_x$. Comparison of the formation energy and change in volume of a bulk PdH$_x$ as a function of H concentration (x), calculated by ACE and DFT.[24]

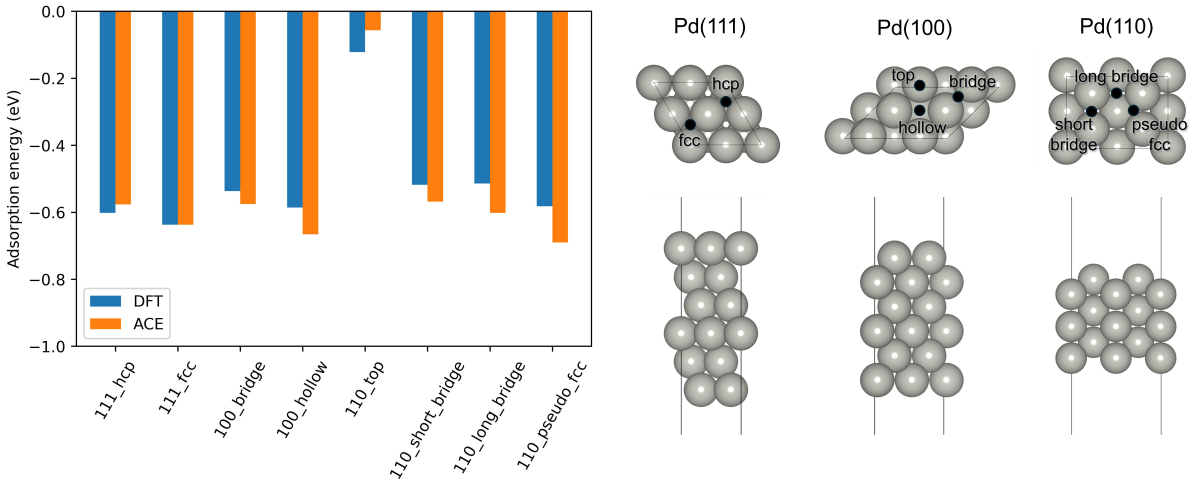

Supplementary Figure 12: Calculated hydrogen adsorption energy on Pd surfaces. Comparison of the H adsorption energy on the Pd(111), Pd(110), and Pd(100) surfaces at various adsorption sites, calculated by ACE and DFT[25] (left panel). The H adsorption sites are also shown for the three Pd slab models (right panel).

Supplementary Section 11: The case of Crystal 4, a larger and non-spherical Pd NC

The measurements of the presented Crystal 4 were performed during another experiment for which slit aperture investigations was not conducted. However, we did take the initial step of setting the photon energy to 20 keV to limit adverse beam-electrolyte interaction.

Crystal 4 measures approximately $350 \times 350 \times 225$ nm^3 in size (see Supplementary Figure **13**). It is larger than Crystal 2 and Crystal 3 but comparable in size to Crystal 5. The NC was probed four times at each potential, twice during a cathodic (negative-going scan) and twice during an anodic (positive-going scan) sweep in the potential range of $0.07 < E < 0.57$ V.

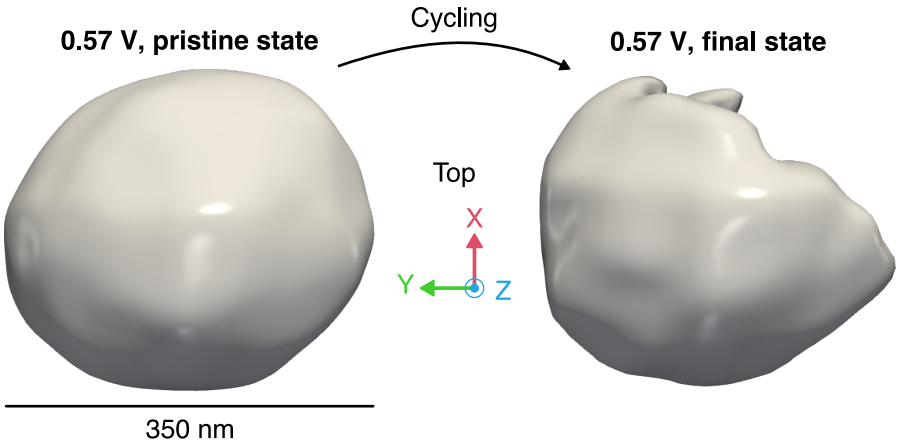

Supplementary Figure 13: **BCDI reconstruction of Crystal 4, measured at** 0.57 **V, before and after potential cycling between** 0.07 **and** 0.57 **V.** A part of the NP is missing after the cycling, suggesting the presence of a structural defect. The missing region does not contribute to the diffraction pattern used to reconstruct the NP and therefore, cannot be reconstructed.

At each potential, the first BCDI measurement was performed almost immediately after switching the potential, followed by the second scan shortly after. For Crystal 4, each scan lasted approximately four minutes. For each BCDI reconstruction of Crystal 4 presented here, we used the data from the second scan, except for the potential at 0.07 V, for which we have included reconstructions from both scans.

The NC did not achieve a full transition to β phase, as the minimal applied potential was too high for the complete transformation to occur. However, we did observe the nucleation of the β phase at 0.07 V, as well as the coexistence of both α and β phases. Furthermore, this NC was reconstructible while both phase coexisted, and consequently exhibited high heterogeneous strain values.

Interestingly, the pristine morphology could not be recovered, which may point towards the emergence of a structural defect, as displayed in Supplementary Fig. **13**. Considering the size of Crystal 4, the nucleation of a defect is consistent with the spherical-cap model, which predicts dislocation formation during the transition at room temperature for nanocrystals larger than approximately 300 nm.[15]

Average lattice parameter evolution

Supplementary Figure **14** displays projections of the diffraction patterns, BCDI reconstructions and changes in the average lattice parameter for the selected electrode potentials. The colouring in the reconstruction indicates the lattice parameter at the voxel level.

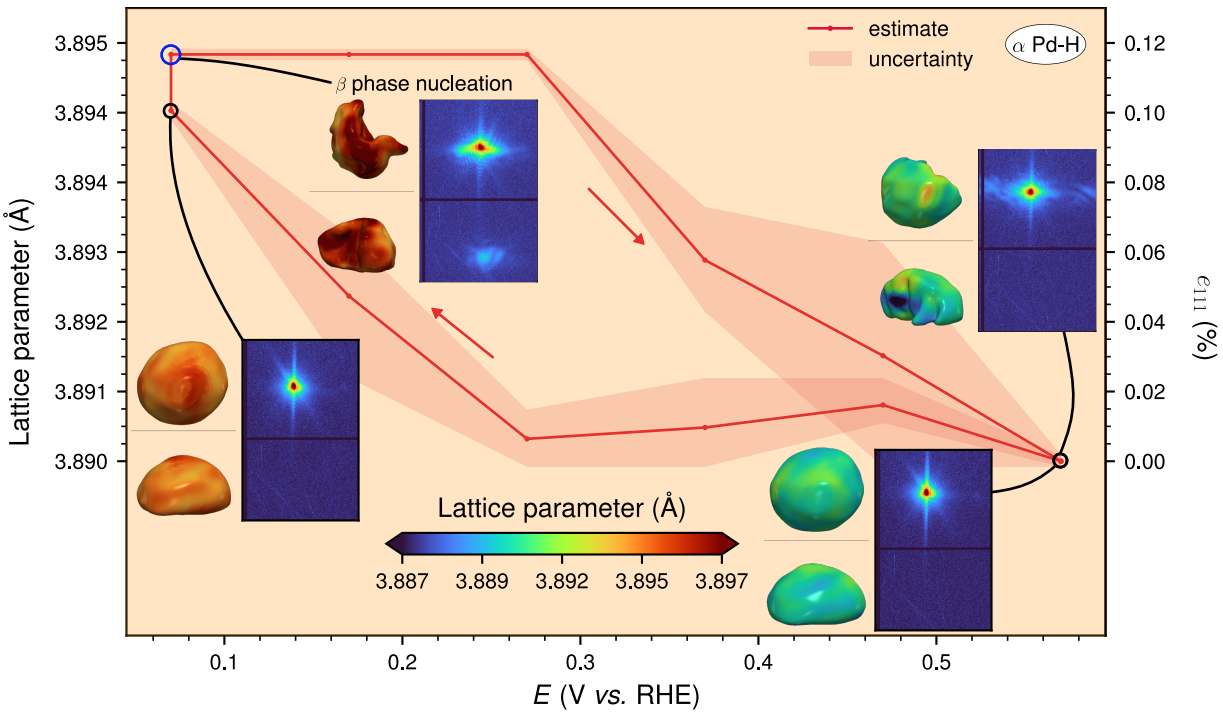

Supplementary Figure 14: Tracking the lattice parameter of Crystal 4 during H insertion/de-insertion. The curve represents the averaged lattice parameter and homogeneous strain evolutions of the Pd nanocrystal as a function of the electrode potential. The reference state is set at 0.57 V. The β phase nucleation is observed at 0.07 V but the full α-to-β transition was not achieved at this potential. Each data point represents the average value of multiple rocking curve measurements, with the uncertainty indicating the range of values. For each selected potential, both top (top) and side (bottom) views of the BCDI reconstructions are provided. The colouring of the reconstructions represents the lattice parameter at each voxel of the NC. The orange background indicates that Crystal 4 was reconstructed exclusively in the α-phase, unlike Crystal 2 where the orange and blue backgrounds indicate reconstructions in both α and β phases.

The two consecutive BCDI scans at 0.07 V are depicted separately in the figure. The first scan was conducted immediately after the potential was applied. Consequently, the NC was out-of-equilibrium

during the first BCDI acquisition, and the BCDI images display two different stages of the α-to-β phase transition. Interestingly, the first diffraction pattern measured at 0.07 V is similar to that measured at 0.57 V, except for a downward shift, indicating an increase in the lattice parameter. The second scan at the same potential shows a significant change in the shape of the diffraction pattern. More importantly, it demonstrates Bragg peak intensity associated with a significantly larger lattice parameter, indicating the presence of some β domain within the NC. This β phase Bragg intensity corresponds to a lattice parameter of 4.031 Å and a lattice mismatch of 3.4 % and 3.6 % with respect to the α phase domain lattice for the same scan and at 0.57 V, respectively.

Additionally, while the lattice parameter remained unchanged after the H insertion/de-insertion cycles, the diffraction pattern at 0.4 V after cycling is significantly wider compared to the initial state, and the corresponding reconstruction shows a missing part. This indicates significant structural changes in Crystal 4.

BCDI reconstructions

Even though both α and β phases coexisted within Crystal 4 at 0.07 V, it was possible to reconstruct the α phase domain, albeit with some difficulty. The total Bragg intensity was cropped around the α phase domain signal before being used in the reconstruction algorithms. This meant that only the Bragg electron density of the α phase domain was reconstructed. Efforts were made to reconstruct both phases, either separately or simultaneously, but the β phase signal was too weak and could not be reliably reconstructed.

The NC's support, used as an initial guess for the reconstruction algorithms, was generated from reconstructions of the NC at a less strained state (0.57 V) to aid in phase retrieval. However, note that the support was not fixed throughout the entire phasing process. Instead, it was updated every 80 iterations during a total of 1230 iterations of ER, HIO, and RAAR (for more details refer to Methods)[2]. The update frequency of the support was intentionally reduced to enhance algorithm stability and reduce the risk of divergence. Furthermore, the support was allowed to shrink only towards the centre of the reconstruction and could not expand. This approach was well-suited for our situation, as we were not interested in reconstructing the β phase domain and only needed to reconstruct a smaller

[2]Usually, when performing phase retrieval, the support is initialised using the autocorrelation of the Bragg intensity. In other terms, this corresponds to the inverse Fourier transform of the measured intensity. In addition, in the generic recipe, we are used to set the support update period to 20, *i.e.* the support is updated according to the real space constraints every 20 iterations.

Bragg electron density within the original support. This method proved effective, yielding multiple satisfactory reconstructions that exhibited consistent morphological features. Ten different runs were utilised to create the final solution.

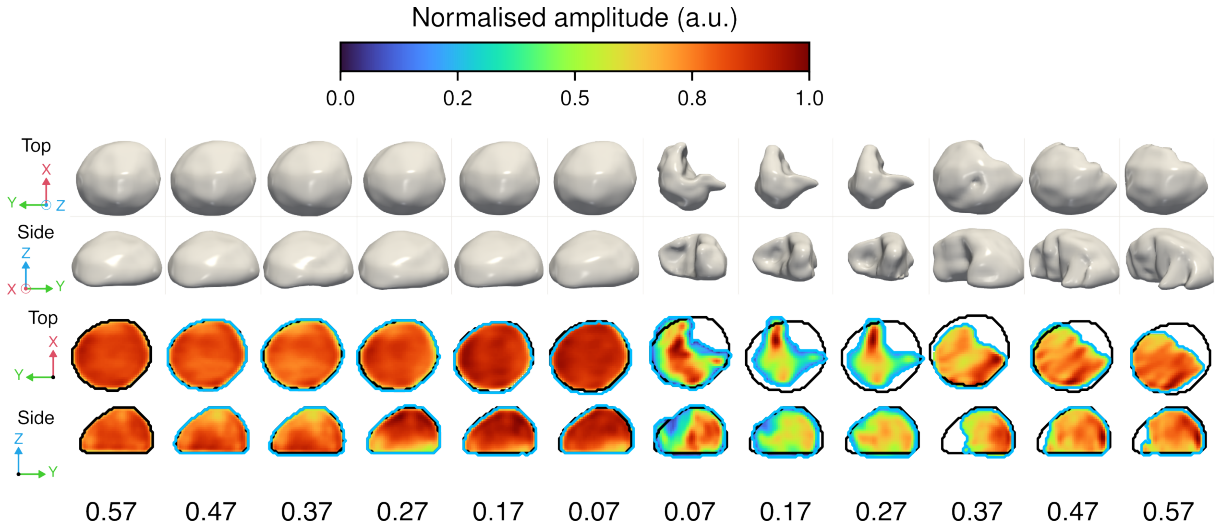

Supplementary Figure 15: Reconstructed Bragg electron density of Crystal 4 as a function of the electrode potential. The first two rows correspond to 3D views. The last two rows represent cross-sections of the normalised reconstructed electron density. The perspectives for the 2D and 3D views are identical.

Supplementary Figure **15** presents both 2D and 3D views of BCDI reconstructions of Crystal 4. The colouring of the cross-sections indicates the normalised reconstructed Bragg electron density. The black contour at 0.57 V represents the pristine contour and is included at each potential for comparison. The 3D views are displayed at various isosurfaces depending on the reconstruction, following the approach outlined in ref.[26]

No significant changes are observed until the first scan at 0.07 V. However, for the second scan at 0.07 V and the two consecutive scans (0.17 and 0.27 V) when both α and β phases coexist, the Bragg electron density within the NC fluctuates, and the contour in the 2D cross-sections changes notably. The missing part in these reconstructions is assumed to correspond to the β phase domain of the NC since the associated Bragg peak intensity was not used for phasing. Intriguingly, when returning to 0.57 V, the morphology does not recover as observed in the truncated cuboctahedra described earlier. Since the lattice parameter remains identical to its pre-cycling state, and the H loading is assumed to be the same, it can be inferred that the previously existing β phase domain has transformed into a grain with a different crystallographic orientation. Consequently, it does not contribute to the diffraction pattern which is why it cannot be reconstructed.

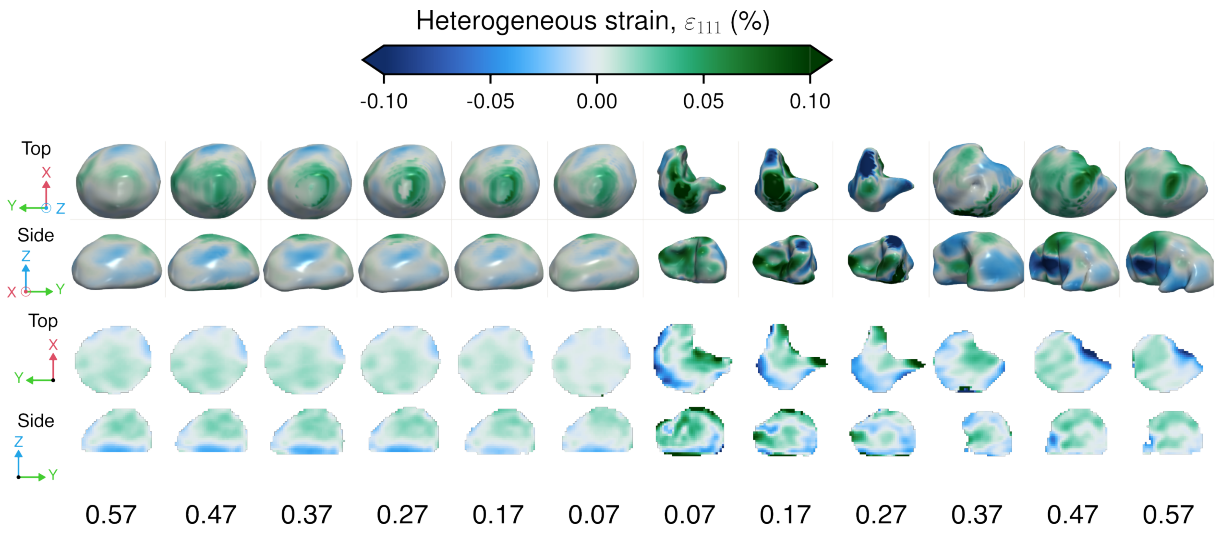

Supplementary Figure 16: 2D and 3D maps of the heterogeneous strain of Crystal 4 as a function of the electrode potential. The first two rows correspond to 3D heterogeneous strain maps. The last two rows represent 2D cross-section of the heterogeneous strain maps. The perspectives for the 2D and 3D views are identical.

Supplementary Figure **16** also presents identical 2D and 3D maps for the same electrode potentials, but the colouring now represents the heterogeneous strain distribution. Importantly, we note that the heterogeneous strain scale used here is significantly larger than those employed previously for the Pd-H system. Heterogeneous strain values now range from -0.1 to 0.1 %, which is much larger than the previous range of -0.03 to 0.03%.

The heterogeneous strain distribution does not undergo significant changes until the second scan at 0.07 V. For each reconstruction before this point, two primary strain features persist across different potentials: compressive strain at the interface with the substrate and tensile strain in the top part of Crystal 4's bulk. However, during the three scans when coexistence occurs, heterogeneous strain values increase substantially. This is expected since two phases with a lattice parameter difference of 3.4% coexist within the same NC. Notably, at the interface between the reconstructed strain and the missing part, there is a large heterogeneous tensile strain, exceeding 0.1 %. These strain values align with the assumption that the missing part is indeed composed of the β phase. Interestingly, at the final state (0.57 V), the heterogeneous strain at the same interface remains large but is inverted, now undergoing compression. This significant compressive heterogeneous strain suggests the presence of a structural defect in this region of the NC.

Similar to Crystal 2, no significant change in heterogeneous strain is observed within the range $[0.07; 0.57]$ V. As discussed previously, we propose that the H-rich surface shell governs the heteroge-

neous strain pattern of the surface in this potential range, explaining the lack of a heterogeneous strain response to (bi)sulfate ion absorption/desorption above 0.07 V.

Lattice parameter analysis

In contrast to the small heterogeneous strain values observed for Crystal 2 (with a maximum value of 0.03 %), significantly larger heterogeneous strain values were detected for Crystal 4 (with a maximum value of 0.1 %). Conversely, the homogeneous strain was found to be twice as large for Crystal 2 (reaching 0.24 % in the α phase regime) compared to Crystal 4 (0.11 %), indicating distinct *d*-spacing behaviours between the two.

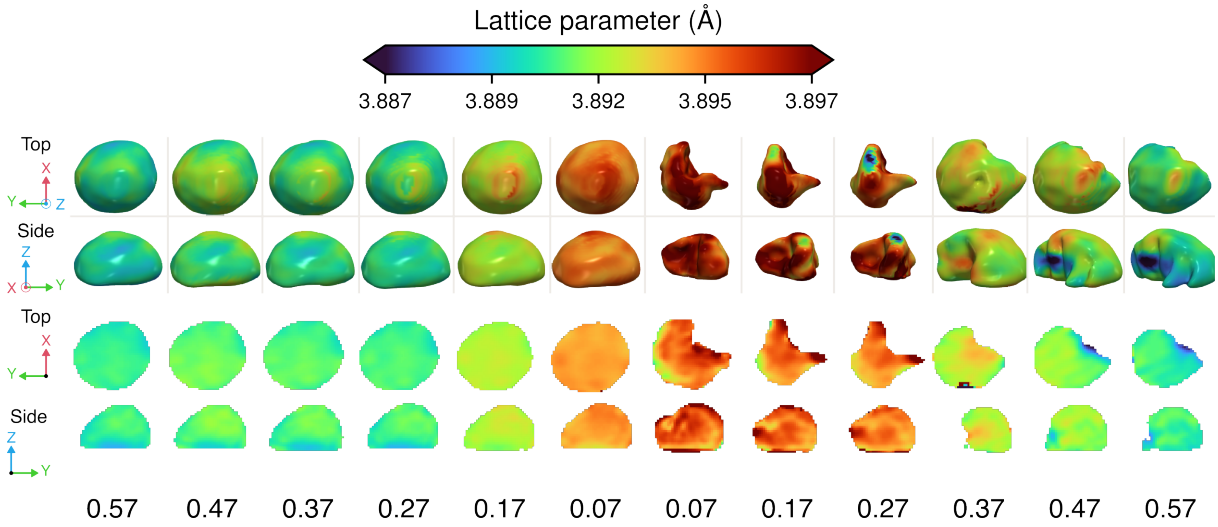

Supplementary Figure 17: 2D and 3D maps of the lattice parameter of Crystal 4 as a function of the electrode potential. The first two rows correspond to 3D lattice parameter maps. The last two rows represent 2D cross-section of the lattice parameter maps. The perspectives for the 2D and 3D views are identical.

As for Crystal 4, due to the coexistence of α and β phases, heterogeneous and homogeneous strain variations have similar orders of magnitude. Consequently, the 3D lattice parameter maps presented in Supplementary Figure **17** encodes equally both variations and appears as a valuable tool to investigate the effect of H insertion in the Pd NC. One can notice that lattice parameter variations occur at 0.17 V, which is before any change in heterogeneous strain occurs. This directly highlights that H insertion initiated between 0.27 and 0.17 V. The average lattice parameter was 3.890 Å at 0.57 V and increased further, reaching 3.895 Å during the first scan and 3.899 Å during the fourth scan at 0.07 V, respectively. Similarly, on return to 0.57 V, the presence of a structural defect has a significant effect on the local lattice parameter, as the compressive strain at the interface reduces the lattice parameter to 3.887 Å.

Supplementary Section 12: Single slice reconstructions of the α phase domain near (at t_0) and upon (at $t_0 + 4$ s) β phase nucleation in Crystal 2

While the complete rocking curve measurement of Crystal 2 at 0.06 V could not be reconstructed, we phased two single slices measured at t_0 and $t_0 + 4$ s. It is worth recalling that the output 2D object corresponds to a projection of the 3D object along the incident beam direction. Supplementary Figure **18** shows the 2D diffraction data, the calculated intensity, and the reconstructed amplitude and phase at t_0 and $t_0 + 4$ s. At t_0, the 2D reconstructed amplitude shape is similar to that of a slice of Crystal 2. At $t_0 + 4$ s, the observed intensity and reconstructed amplitude values are lower in magnitude than those measured at t_0, indicating a reduction of the diffracting α phase domain. This suggests the coexistence of both phases within Crystal 2, which is also evidenced by the distinct shapes of the 2D reconstructed amplitudes.

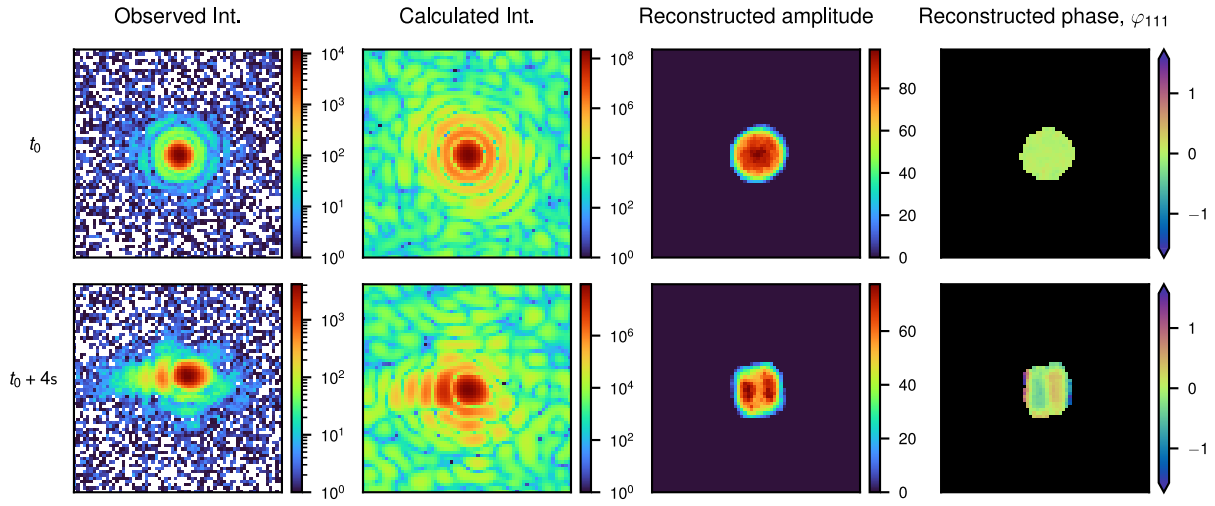

Supplementary Figure 18: **Single slice reconstructions near (at t_0) and upon (at $t_0 + 4$ s) β phase nucleation for Crystal 2.**

While the 2D reconstructed phases are challenging to interpret, as they contain information about the entire volume, the particular signature of the phase slice measured at $t_0 + 4$ s is intriguing. Supplementary Figure **19** displays horizontal line profiles of the phase measured at $t_0 + 4$ s taken at various heights of the reconstruction. The horizontal line profiles all show a wave-shaped signature –decrease, increase, decrease– of the phase along the horizontal direction. Along with the highly asymmetric Bragg peak, this rapidly varying phase field may indicate the presence of a defect, such as a dislocation,

outside of the α phase domain. Therefore, an attempt to reproduce a similar phase field is provided in Supplementary Figure **19**.

To simulate the phase field, multiple 3D phase objects containing a phase vortex with various (dislocation) orientations. In each case, the dislocation position was set outside of the reconstructed support to simulate a dislocation in the β phase, at the α-β phase interface, or whithin the subsurface layers of the hydride as suggested by ref.[23] The 3D objects are then summed along one direction, which corresponds to the rocking curve direction, to generate the slice object.

We selected the phase dislocation orientation that approximately matches our observed 2D phase field. Slices of the 3D phase object used to simulate the phase field in Supplementary Figure **19** are displayed in Supplementary Figure **20**. A complex object is further simulated by imposing the 2D reconstructed amplitude, and the associated Fourier transform is computed. While the calculated 2D diffraction patterns show differences, asymmetry along the horizontal direction can still be observed.

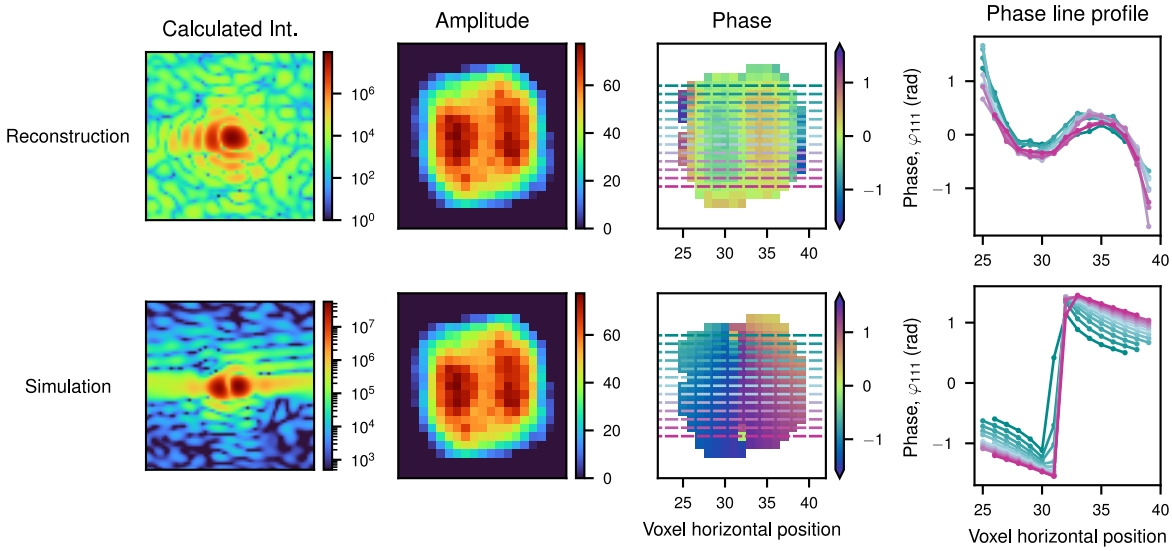

Supplementary Figure 19: Simulation of the observed 2D phase field at $t_0 + 4$ s using a phase vortex outside of the reconstructed support for Crystal 2.

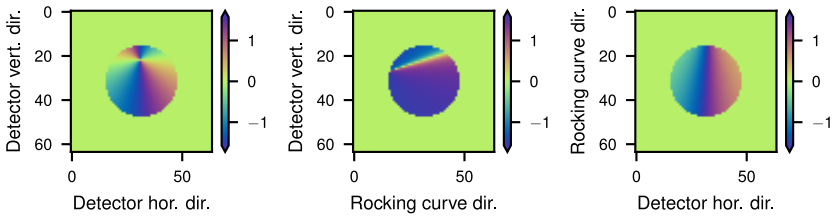

Supplementary Figure 20: 3D spherical phase object used to generate the phase field.

Supplementary Section 13: The case of Crystal 5, coherent α-to-β phase transformation

Crystal 5 was investigated under 'fast' rocking curve scans in order to capture information in the reciprocal space. Before conducting the series of measurements, a typical BCDI rocking curve scan was performed. Supplementary Figure **21** displays reconstruction of Crystal 5 from different perspectives. Note Crystal 5 is significantly larger than Crystal 2 and the associated surface heterogeneous strain pattern significantly less structured than the other NCs. This NC is [002]-oriented, has a different facet distribution, and therefore exhibits a different surface strain signature.

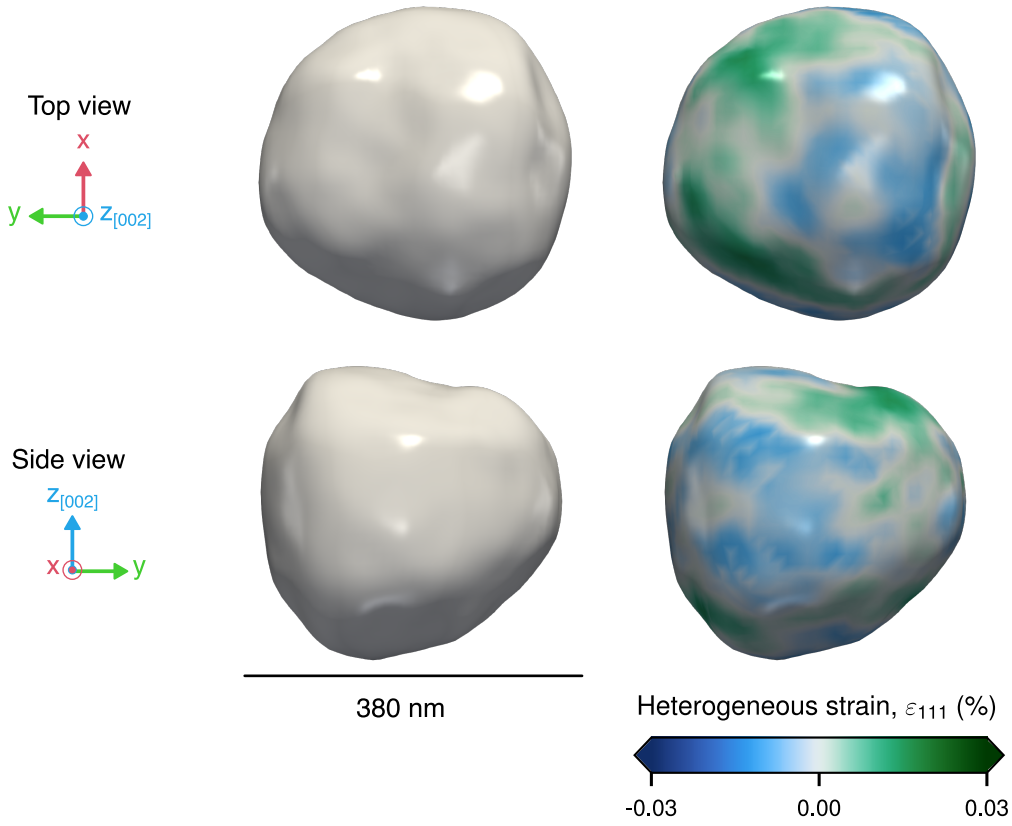

Supplementary Figure 21: **Reconstruction of Crystal 5 at 0.7 V.** Crystal 5 is [002]-oriented, has dimensions of $360 \times 380 \times 380$ nm^3 and exhibits a markedly different heterogeneous strain signature compared to other [111]-oriented crystals.

The fast scans were conducted every 3 seconds, consisting of 30-frame rocking curves spanning a 1-degree angle range. Each frame had a counting time of 0.2 seconds, resulting in a total exposure time of 6 seconds. For this particular NC, the transition was observed at 0.03 V, slightly lower than that observed for Crystal 2. This difference could be attributed to the difference in size and the notably

reduced beam-induced radiolysis due to the low total exposure time per scan of 6 seconds (also note that slit aperture was fixed to $60 \times 60\ \mu m^2$).

Upon β phase nucleation, an upward shift of the α phase domain Bragg peak is observed, indicating a reduction in lattice parameter, consistent with observations for Crystal 2 and Crystal 1. During the α-to-β phase transition, intensity is detected in the intermediate region between the two phase peak regions before a clear and distinct intensity is seen in the β phase region. This suggests a coherent α-to-β phase transition, with intermediate lattice parameter values. Additionally, the remaining α domain Bragg peak appears significantly less strained compared to when the transition is not coherent.

On the anodic sweep, the β-to-α phase transition begins at 0.08 V, but this time, no intensity is observed between the two regions. The diffracted intensities indicate significantly more strongly strained domains. This observation aligns with the expectation that if no lattice parameter adjustment occurs to accommodate the mismatch, both domains experience high strain. We note that this scenario is described by Griessen and colleagues' model in Supplementary Section 13 of Supplementary Information, Scenario II, in ref.[27] The scenario involves a coherent core-surface-shell α-to-β phase transition and incoherent core-surface-shell β-to-α phase transition. Finally, note that we could not recover Crystal 5's pristine diffraction pattern at 0.7 V.

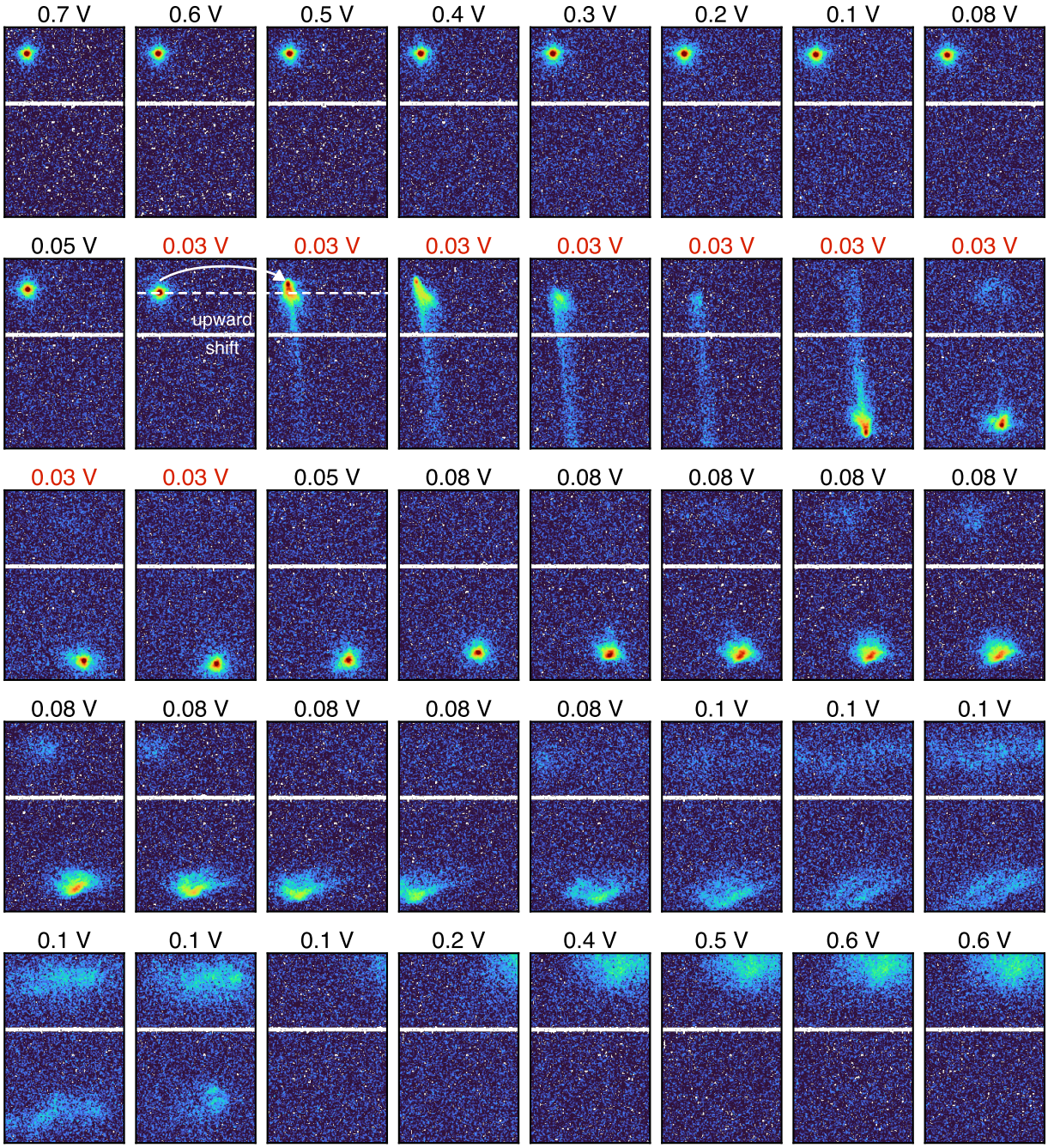

Supplementary Figure 22: **Diffraction tracking of Crystal 5 during H insertion/de-insertion.** The values of potential coloured in red indicate the potential of β phase nucleation and α-to-β phase transition. Upon β phase nucleation, the α phase domain Bragg peak shifts upwards as observed for Crystal 2 and Crystal 1. Continuous intensity between the α and β regions can only be seen for the α-to-β phase transition. Potentials are indicated versus RHE.

References

(1) Vasile, M. J.; Enke, C. G. The Preparation and Thermodynamic Properties of a Palladium-Hydrogen Electrode. *Journal of The Electrochemical Society* **1965**, *112*, 865.

(2) Jerkiewicz, G. Hydrogen sorption ATIN electrodes. *Progress in Surface Science* **1998**, *57*, 137–186.

(3) Chattot, R.; Martens, I.; Mirolo, M.; Ronovsky, M.; Russello, F.; Isern, H.; Braesch, G.; Hornberger, E.; Strasser, P.; Sibert, E.; Chatenet, M.; Honkimäki, V.; Drnec, J. Electrochemical Strain Dynamics in Noble Metal Nanocatalysts. *Journal of the American Chemical Society* **2021**, *143*, 17068–17078.

(4) Łukaszewski, M.; Czerwiński, A. The method of limited volume electrodes as a tool for hydrogen electrosorption studies in palladium and its alloys. *Journal of Solid State Electrochemistry* **2011**, *15*, 2489–2522.

(5) Viola, A.; Chattot, R.; Martin, V.; Tsirlina, G.; Nelayah, J.; Drnec, J.; Maillard, F. Hydrogen Trapping in Palladium Nanoparticles Revealed by Electrochemical, X-ray Scattering, and Spectrometric Measurements. *The Journal of Physical Chemistry C* **2023**, *127*, 17761–17769.

(6) Wolfe, R. C.; Weil, K. G.; Shaw, B. A.; Pickering, H. W. Measurement of pH Gradients in the Crevice Corrosion of Iron Using a Palladium Hydride Microelectrode. *Journal of The Electrochemical Society* **2005**, *152*, B82.

(7) Björling, A.; Marçal, L. A. B.; Arán-Ais, R. M.; Solla-Gullón, J. Chemical Limits on X-ray Nanobeam Studies in Water. *The Journal of Physical Chemistry C* **2023**,

(8) Thomas, J. K. Rates of reaction of the hydroxyl radical. *Transactions of the Faraday Society* **1965**, *61*, 702–707.

(9) Thomas, J. K.; Rabani, J.; Matheson, M. S.; Hart, E. J.; Gordon, S. Absorption Spectrum of the Hydroxyl Radical1. *The Journal of Physical Chemistry* **1966**, *70*, 2409–2410.

(10) Sehested, K.; Christensen, H. The rate constant of the biomolecular reaction of hydrogen atoms at elevated temperatures. *International Journal of Radiation Applications and Instrumentation. Part C. Radiation Physics and Chemistry* **1990**, *36*, 499–500.

(11) Mezyk, S. P.; Bartels, D. M. Direct EPR measurement of Arrhenius parameters for the reactions of H˙ atoms with H2O2 and D˙ atoms with D2O2 in aqueous solution. *Journal of the Chemical Society, Faraday Transactions* **1995**, *91*, 3127–3132.

(12) NIST: X-Ray Mass Attenuation Coefficients - Water, Liquid. `https://physics.nist.gov/PhysRefData/XrayMassCoef/ComTab/water.html`.

(13) Durst, J.; Siebel, A.; Simon, C.; Hasché, F.; Herranz, J.; Gasteiger, H. A. New insights into the electrochemical hydrogen oxidation and evolution reaction mechanism. *Energy & Environmental Science* **2014**, *7*, 2255–2260, Publisher: The Royal Society of Chemistry.

(14) Sherbo, R. S.; Moreno-Gonzalez, M.; Johnson, N. J. J.; Dvorak, D. J.; Fork, D. K.; Berlinguette, C. P. Accurate Coulometric Quantification of Hydrogen Absorption in Palladium Nanoparticles and Thin Films. *Chemistry of Materials* **2018**, *30*, 3963–3970.

(15) Ulvestad, A.; Welland, M. J.; Cha, W.; Liu, Y.; Kim, J. W.; Harder, R.; Maxey, E.; Clark, J. N.; Highland, M. J.; You, H.; Zapol, P.; Hruszkewycz, S. O.; Stephenson, G. B. Three-dimensional imaging of dislocation dynamics during the hydriding phase transformation. *Nature Materials* **2017**, *16*, 565–571.

(16) Prakash, A.; Hummel, M.; Schmauder, S.; Bitzek, E. Nanosculpt: A methodology for generating complex realistic configurations for atomistic simulations. *MethodsX* **2016**, *3*, 219–230.

(17) Thompson, A. P.; Aktulga, H. M.; Berger, R.; Bolintineanu, D. S.; Brown, W. M.; Crozier, P. S.; in 't Veld, P. J.; Kohlmeyer, A.; Moore, S. G.; Nguyen, T. D.; Shan, R.; Stevens, M. J.; Tranchida, J.; Trott, C.; Plimpton, S. J. LAMMPS - a flexible simulation tool for particle-based materials modeling at the atomic, meso, and continuum scales. *Comp. Phys. Comm.* **2022**, *271*, 108171.

(18) Favre-Nicolin, V.; Coraux, J.; Richard, M.-I.; Renevier, H. Fast computing of scattering maps of nanostructures using graphical processing units. *J. Appl. Cryst.* **2011**, *44*, 635–640.

(19) Atlan, C.; Chatelier, C.; Olson, K. A python package to help Coherent Diffraction Imaging (CDI) practitioners in their analysis. 2023.

(20) Lysogorskiy, Y.; Oord, C. v. d.; Bochkarev, A.; Menon, S.; Rinaldi, M.; Hammerschmidt, T.; Mrovec, M.; Thompson, A.; Csányi, G.; Ortner, C.; others Performant implementation of the atomic

cluster expansion (PACE) and application to copper and silicon. *npj computational materials* **2021**, *7*, 97.

(21) Drautz, R. Atomic cluster expansion for accurate and transferable interatomic potentials. *Physical Review B* **2019**, *99*, 014104.

(22) Bochkarev, A.; Lysogorskiy, Y.; Menon, S.; Qamar, M.; Mrovec, M.; Drautz, R. Efficient parametrization of the atomic cluster expansion. *Physical Review Materials* **2022**, *6*, 013804.

(23) Ngoipala, A. et al. Hydride-Induced Reconstruction of Pd Electrode Surfaces: A Combined Computational and Experimental Study. *Advanced Materials* **2024**, 2410951.

(24) Schmidt, T. O.; Ngoipala, A.; Arevalo, R. L.; Watzele, S. A.; Lipin, R.; Kluge, R. M.; Hou, S.; Haid, R. W.; Senyshyn, A.; Gubanova, E. L.; Bandarenka, A. S.; Vandichel, M. Elucidation of Structure–Activity Relations in Proton Electroreduction at Pd Surfaces: Theoretical and Experimental Study. *Small* **2022**, *18*, 2202410.

(25) Ngoipala, A.; Lipin, R.; Arevalo, R. L.; Vandichel, M. Computational unravelling of cathodic hydride formation on palladium surfaces. *International Journal of Hydrogen Energy* **2024**, *53*, 829–839.

(26) Carnis, J.; Gao, L.; Labat, S.; Kim, Y. Y.; Hofmann, J. P.; Leake, S. J.; Schülli, T. U.; Hensen, E. J. M.; Thomas, O.; Richard, M.-I. Towards a quantitative determination of strain in Bragg Coherent X-ray Diffraction Imaging: artefacts and sign convention in reconstructions. *Scientific Reports* **2019**, *9*, 17357.

(27) Griessen, R.; Strohfeldt, N.; Giessen, H. Thermodynamics of the hybrid interaction of hydrogen with palladium nanoparticles. *Nature Materials* **2016**, *15*, 311–317.